

## Radio emission across the entire rotation phases of pulsars

P. F. WANG<sup>1,2</sup> AND J. L. HAN<sup>1,2</sup>

<sup>1</sup>National Astronomical Observatories, Chinese Academy of Sciences, 20A Datun Road, Chaoyang District, Beijing 100101, China

<sup>2</sup>School of Astronomy, University of Chinese Academy of Sciences, Beijing 100049, China

### ABSTRACT

Super-sensitive observations of bright pulsars by the Five-hundred-meter Aperture Spherical radio Telescope (FAST) have revealed weak radio emission continuously emerged in the rotation phases between the main pulse and interpulse of an rotating neutron star. We develop a model for the polarized radio emission radiated from different heights in the pulsar magnetosphere and examine emission intensity distribution over the whole rotation phases of pulsars seen from all directions by the line of sight. We find that for pulsars with small periods and the magnetosphere filled with much more relativistic particles, the polarized radio emission can be generated in all rotation phases for both the aligned and perpendicular rotating neutron stars. When the line of sight cuts the pulsar emission beam between the rotation and magnetic axes, the polarization angles have the same sense of variation gradient for the “main” pulse and “interpulse”. If the line of sight cuts the beams between the inclined magnetic axis and the equator, the opposite senses can be found for the main pulse and interpulse. In addition to the pulsed emission, we find persistent radio emission generated in the pulsar magnetosphere. The model can naturally explain the emission across the entire rotation phases.

*Keywords:* pulsars: general

### 1. INTRODUCTION

The mean polarization profiles of pulsars reflect the emission geometry and emission processes in the magnetosphere of neutron stars. Radio observations can give details of polarization profiles (e.g. Gould & Lyne 1998; Han et al. 2009; Posselt et al. 2023; Wang et al. 2023). In general, pulsars have profiles with a duty cycle of about several percent of the rotational phase. Some pulsars have wide profiles with emission in the phase of more than 180° and even full of all the rotation phases up to almost 360°, such as PSRs J1916+0748 and J2007+2722 (Wang et al. 2023). The profiles typically have one, two, three, or more components, and are often linearly and circularly polarized. The polarization position angles of some pulsars exhibit a S-shaped curve or have orthogonal modes at some phases. In addition to conventionally detected pulses, some pulsars may have persistent radio emission as revealed by the aperture synthesis mapping observations (Gautam et al. 2022).

Some empirical or physical models have been proposed to understand diverse pulsar profiles. The observed polarization profiles are related to pulsar geometry (Radhakrishnan & Cooke 1969), emission mechanisms (e.g. Xu et al. 2000), propagation effects (e.g. Arons & Barnard 1986; Wang et al. 2010; Beskin & Philippov 2012) or their combination (Wang et al. 2014b). They result from the cutting of pulsar emission

beams by sight lines. The beams may have a shape in circular (Lyne & Manchester 1988; Gil & Han 1996), or elongated in the meridional plane direction (Narayan & Vivekanand 1983), or compressed along which (Biggs 1990; Qiao et al. 2004; Gangadhara 2004). Profile components originate from the radiation beams that might have configurations of a conal and/or core (Rankin 1983), or patchy (e.g. Lyne & Manchester 1988; Han & Manchester 2001), or fan-shaped (e.g. Wang et al. 2014a). It is very hard to reveal the real shape and configuration of the emission beam of one pulsar. The procession of the rotation axis of some binary pulsars, such as PSR J1906+0746, indeed provides us a chance to figure out some part of the emission beam (Desvignes et al. 2019) by using observations over many years.

Curvature radiation is one of the most probable mechanisms for pulsar radiation, and has been taken to interpret pulsar polarization (e.g. Gil & Snakowski 1990). When the detailed emission geometry and particle distributions are taken into account, the swing of polarization position angle curves and circular polarization can be naturally produced, as shown by simulations (Gangadhara 2010; Wang et al. 2012). Previously, most pulsar emission models are confined to emission generated from a fixed height of pulsar magnetosphere and detected by a given sight line. The polarized emission from the entire magnetosphere has not yet been explored.

In this paper, we develop a model by accounting for the curvature radiation from the entire pulsar magnetosphere to

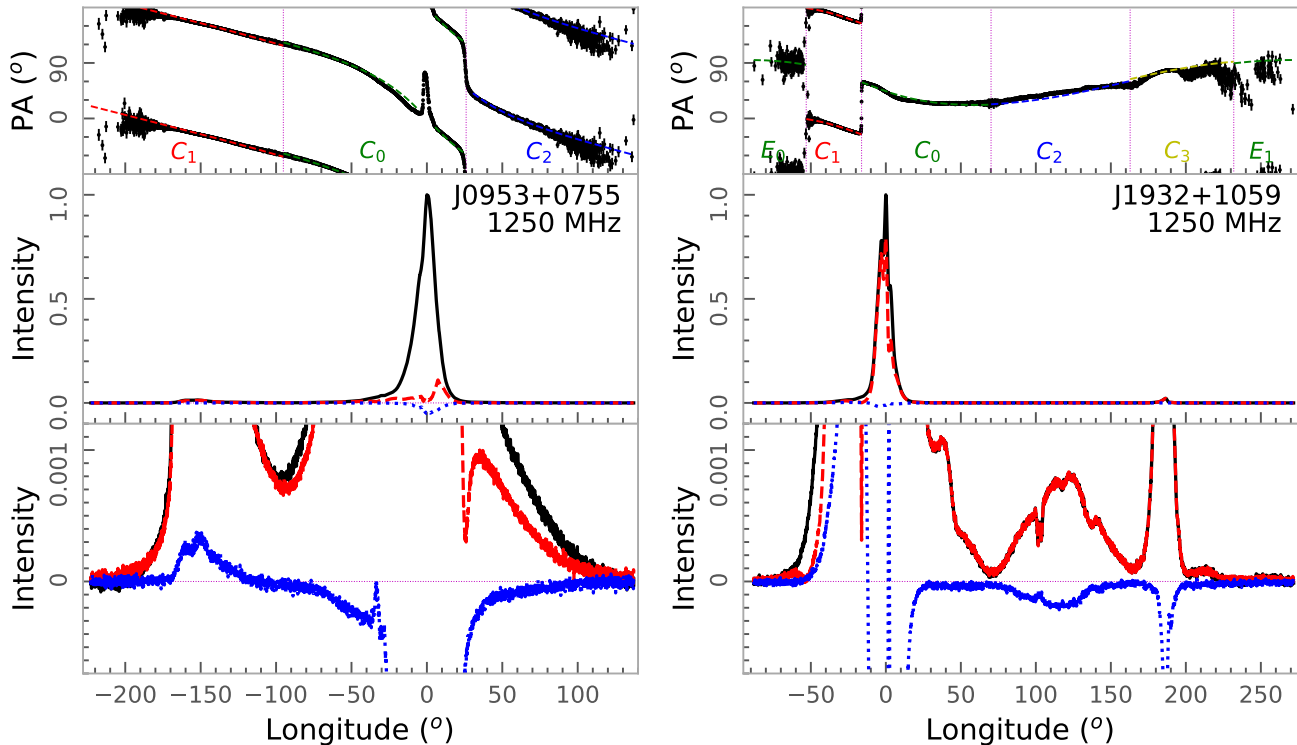


**Figure 1.** Mean polarization profiles of PSRs J0953+0755 and J1932+1059. The total intensity, linear and circular polarization intensities are represented by solid line, dashed line and dotted line in the bottom and middle sub-panels for each pulsar, while the bottom sub-panels are zoomed to show weak parts of profiles. Polarization position angles are shown in the top sub-panels by dots with error-bars for data of linear polarization intensity greater than  $3\sigma$ . The piecewise RVM fitting is performed to the PAs in three phase ranges ( $C_0$ ,  $C_1$  and  $C_2$ , as separated by the vertical dashed lines) for PSR J0953+0755 with orthogonal mode jump modelled for  $C_2$ , and four ranges ( $C_0$ ,  $C_1$ ,  $C_2$  and  $C_3$ ) for PSR J1932+1059 with  $C_1$  having orthogonal mode jump modelled. The two ranges ( $E_0$  and  $E_1$ ) with very weak emission and PAs with large uncertainties for PSR J1932+1059 are not modeled, but the predicted PA curve is plotted.

explain the weak emission detected from the whole phase of pulsar rotation. We first present the sensitive FAST observations of bright pulsars to show the weak emission generated within one pole or between two poles of the beam in Section 2. In Section 3, we set the model assumptions, and present the simulation methods and results from a static pulsar magnetosphere. In Section 4, we compare the model to observations. Discussion and conclusions are given in Section 5.

## 2. RADIO EMISSION OVER WIDE ROTATION PHASES OF TWO PULSARS

Here we consider two bright pulsars, PSRs J0953+0755 and J1932+1059, which have been observed by the Five-hundred-meter Aperture Spherical radio Telescope (FAST) (Nan 2006). The weak polarized emission in a wide rotation phase range or the entire phase between the two magnetic poles has been well-detected.

The bright PSR J0953+0755 is one of the first few pulsars ever discovered (Pilkington et al. 1968), which has a spin period of 0.253s and has the emission detected in almost all the rotation phases in the frequencies from 55 MHz to 1425 MHz (e.g. Hankins & Cordes 1981; McLaughlin & Rankin 2004; Bilous et al. 2022; Wang et al. 2022). There

was no consensus on the emission coming from the beam of one magnetic pole (Narayan & Vivekanand 1983; Lyne & Manchester 1988; Blaskiewicz et al. 1991; Rankin 1993) or two poles (Everett & Weisberg 2001).

PSR J1932+1059 is also very bright. It was discovered during Molonglo pulsar search (Large et al. 1968) and has a spin period of 0.226 s. The main pulse and the interpulse are separated by  $180^\circ$  which is most likely generated from two poles (Rankin & Rathnasree 1997). The bridge emission between the main pulse and interpulse has been detected at 408, 430, 1170, 1250 and 1665MHz (Perry & Lyne 1985; Phillips 1990; McLaughlin & Rankin 2004; Kou et al. 2021). Because of the bridge emission, it has been argued to originate from a single pole (e.g. Lyne & Manchester 1988; Phillips 1990).

Emission geometries of these two pulsars have been investigated through either the empirical beam-analysing method (Lyne & Manchester 1988; Rankin 1993) or fitting to the polarization position angle curves with the rotating vector model (RVM) (e.g. Phillips 1990; Blaskiewicz et al. 1991; Everett & Weisberg 2001). The geometric parameters derived by previous authors (and also this work, see below) are listed in Table 1.

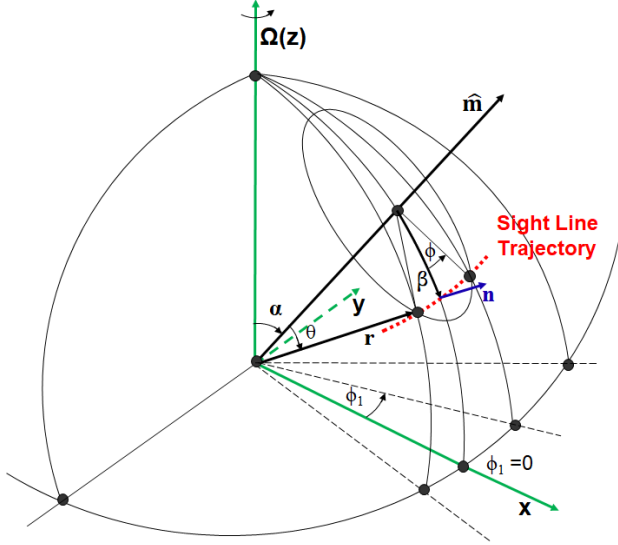


**Figure 2.** Geometry of pulsar magnetosphere. The magnetic axis  $\hat{m}$  is inclined at an angle of  $\alpha$  with respect to the rotation axis  $\Omega$ . The line of sight  $\hat{n}$  cuts across the emission beam with an impact angle  $\beta$  from the magnetic axis, whose trajectory is indicated by the dotted arc. The line of sight always has an angle of  $\zeta = \alpha + \beta$  with respect to the rotation axis, so that it is named as being the sight line angle. We use  $\alpha_0 = 180^\circ - \alpha$ ,  $\beta_0 = -\beta$  and  $\zeta_0 = 180^\circ - \zeta$  to mark the values derived from observations. A given emission position in the magnetosphere can be described by three parameters:  $r$ ,  $\theta$  and  $\phi$  with respect to the magnetic axis frame. In the rotation axis frame with the z-axis along the rotation axis, the x-axis lies in the meridional plane defined by the magnetic and rotation axes and the rotation phase is indicated by  $\phi_1$ .

The FAST observations of these two pulsars were carried out on 2022 August 29th and 2022 November 21th respectively for 6442 seconds each by using the central beam of the L-band 19-beam receiver. The receiver covers the frequency range of 1.0-1.5 GHz, and has a system temperature of about 22 K (Jiang et al. 2020). Signals from the receiver were digitally channelized to 4096 frequency channels, and then sampled at a time resolution of  $49.152\mu s$  for the 4 polarization channels,  $XX$ ,  $YY$ ,  $\text{Re}[X^*Y]$  and  $\text{Im}[X^*Y]$ . The recorded FAST data were dedispersed and folded. Polarization calibrated following the procedures described by (Wang et al. 2023). In short, the gain, differential gain and differential phase in the two polarization  $X$  and  $Y$  are calibrated by using injected noise diode signals recorded before or after the observation session. Because the receiver has the XY feed, the polarization leakage has been tested and found to be less than 0.03% (Ching et al. 2022).

We obtained the mean polarization profiles of the two pulsars as shown in Figure 1. They come from the most sensitive observations ever available and have a dynamical range of more than 20000. The profile details at a level of 1/10000 the peak intensity can even be detected with a very high signal-to-noise ratio (S/N), which locate at the rotation phases be-

**Table 1.** Geometry parameters of PSRs J0953+0755 and J1932+1059.

$\alpha_0$ ( $^\circ$ )	$\beta_0$ ( $^\circ$ )	Freq. (GHz)	Ref.
PSR J0953+0755			
170	5	0.43	1
174.1	4.2	0.4	2
174(90)	2.5(40)	0.43	3
174(30)	2.5(15)	1.42	3
168	8.5	1.0	4
179.3(150)	1.0(150)	1.41	5
153.1(900)	4.1(50)	4.85	5
105.4(5)	22.1(1)	1.42	7
PSR J1932+1059			
35	23	0.43	1
6	4	0.4	2
25(2)	16(2)	0.43	3
27(4)	16(3)	1.42	3
90	41.8	1.0	4
41(8)	21(4)	0.41	6
51(3)	35(3)	0.61	6
61(2)	39(2)	1.41	6
36(1)	25.6(9)	1.42	7

**References**—1: Narayan & Vivekanand (1982); 2: Lyne & Manchester (1988); 3: Blaskiewicz et al. (1991); 4: Rankin (1993); 5: von Hoensbroech & Xilouris (1997); 6: Stairs et al. (1999); 7: Everett & Weisberg (2001);

tween the main pulse and inter-pulse<sup>1</sup>. Similar results have also been shown by Wang et al. (2022) and Kou et al. (2021).

PSR J0953+0755 has a wide profile over  $310^\circ$  phase at the level of 1/10000 the peak intensity, as shown in Figure 1. The interpulse is about  $150^\circ$  ahead of the main pulse, with an intensity of 2% the main pulse peak. The continuous bridge emission between the main pulse and the interpulse is highly polarized, and has an intensity of only about 1/1000 the main pulse, but clearly detected by FAST. Compared with previous results obtained from Arecibo observations (McLaughlin & Rankin 2004), the new profiles in Figure 1 show the weak interpulse emission at the longitude of  $-150^\circ$  and even weaker bridge emission between the two peaks, extending almost  $360^\circ$  of the rotation phases. Because emission at different phases originates from various heights in the pulsar magnetosphere, the rotation-induced distortion of polar-

<sup>1</sup> Here, we set the lowest points of the profiles as the zero-level for the baseline, assuming that the flux densities there go to zero. It is possible that there is still emission at these phases and even polarized. If so such a possible offset would distort the presented position angles more severely for the lower level polarized emission.

ization position angles therefore can be different (e.g. Dyks 2008; Wang et al. 2012) and the traditional RVM is hard to describe the PA variations over the whole rotation phase. We therefore develop a new piecewise RVM, as described in the Appendix A, to fit the PA curve. As shown in Figure 1, the piecewise RVM can fit the observed PA values well. The precise geometry parameters can therefore be determined, which are  $\alpha_0 = 177.3^{+1.3}_{-1.7}$  degrees for the inclination angle and  $\zeta_0 = 178.3^{+0.8}_{-1.0}$  degrees for the sight line angle, as listed in Table 1. This pulsar is an aligned rotator.

The sensitive FAST observation of PSR J1932+1059 also revealed the highly polarized continuous bridge emission between the interpulse and main pulse, with an intensity of only 1/1000 of the main pulse, see Figure 1. Compared with previous results from the Arecibo observations at 1170 MHz (McLaughlin & Rankin 2004), the trailing part of profiles in the phase range of  $C_3$  has been clearly detected, and emission in the ranges of  $E_0$  and  $E_1$  can be seen. We use the piecewise RVM to fit the PA variations, and get the geometrical parameters of  $\alpha_0 = 33.8^{+1.6}_{-2.2}$  and  $\zeta_0 = 69.6^{+5.5}_{-6.4}$  degrees, demonstrating that this pulsar is an orthogonal rotator.

### 3. A MODEL FOR POLARIZED RADIO EMISSION FROM A STATIC PULSAR MAGNETOSPHERE

To understand radio emission generated from any height at any rotation phase of pulsar magnetosphere, we here do simulations and examine the projected emission on the sky.

#### 3.1. Assumptions used in simulations

We assume that the magnetosphere of a pulsar is a static dipole, within which relativistic particles stream out from the two magnetic poles along the curved magnetic field lines and radiate via curvature emission mechanism.

##### 3.1.1. Dipole geometry

The magnetic field of a pulsar is assumed to be an inclined dipole field,

$$\mathbf{B} = B_* \left( \frac{R_*}{r} \right)^3 [3\hat{\mathbf{r}}(\hat{\mathbf{r}} \cdot \hat{\mathbf{m}}) - \hat{\mathbf{m}}]. \quad (1)$$

Here,  $B_*$  and  $R_*$  are the surface magnetic field and neutron star radius,  $\hat{\mathbf{m}}$  is unit vector along the magnetic axis  $\mathbf{m}$ ,  $\hat{\mathbf{r}}$  represents the unit vector along  $\mathbf{r}$  with an amplitude of

$$r = r_e \sin^2 \theta. \quad (2)$$

Here  $r_e$  is the field line constant and  $\theta$  is the polar angle of a point on a given magnetic field line with respect to the magnetic axis. Considering a magnetic dipole moment  $\mathbf{m}$  inclined with an angle of  $\alpha$  with respect to the rotation axis  $\Omega$  as shown in Figure 2, the parameterization of  $\mathbf{r}$  and  $\hat{\mathbf{m}}$  in a Cartesian coordinate system with the z-axis along  $\Omega$  can be found from Equations (1), (2) and (3) of Gangadhara (2004).

Pulsar radio emission is generally deemed to be generated from the open magnetic field line region of pulsar magnetosphere. As bounded by the light cylinder, the open field

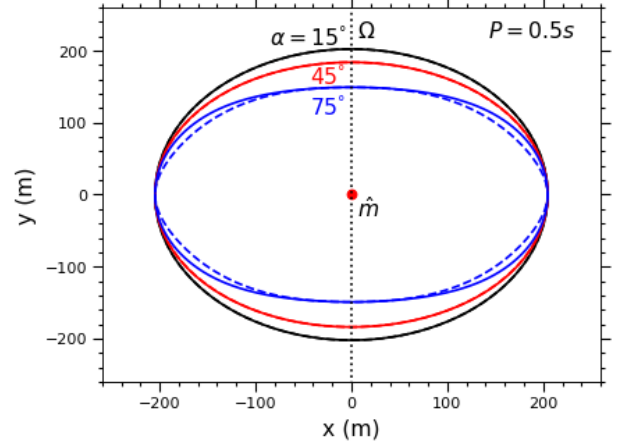


**Figure 3.** Polar cap shape for a pulsar rotating with a period of 0.5s. The polar cap is centered around the magnetic axis  $\hat{\mathbf{m}}$ . The meridional plane defined by the magnetic and rotation axes is indicated by the black dotted line. The black, red and blue lines are for polar caps with  $\alpha = 15^\circ$ ,  $45^\circ$  and  $75^\circ$ . The solid and dashed lines represent polar caps calculated with vector and projection methods, respectively.

lines have a minimum of  $r_e$  within a given magnetic field line plane  $\phi$ , which is denoted as  $r_{e,\text{lof}}$  and can be calculated with the vector or projection methods. In the *Vector method*, the last open magnetic field lines are considered as a sphere that is tangential to the light cylinder. At the tangent point, the cross product of the differential vectors of  $\mathbf{r}$  is perpendicular to the rotation axis, i.e.,  $(\frac{\partial \mathbf{r}}{\partial \theta} \times \frac{\partial \mathbf{r}}{\partial \phi}) \cdot \hat{\Omega} = 0$ . By solving for the polar angle  $\theta_t$  of the tangent point, one can get  $r_{e,\text{lof}}$  as demonstrated by Equations (13), (14) and (15) of Gangadhara (2004). In the *Projection method*, a curved magnetic field line is tangential to the light cylinder at the position  $\mathbf{r}_t$ , which has a component  $r_p$  perpendicular to the rotation axis with a magnitude of  $cP/2\pi$ . The  $r_{e,\text{lof}}$  can be obtained by solving  $dr_p/d\theta = 0$ , as depicted by Equations (7), (8) and (9) of Zhang et al. (2007).

Foot points of the last open magnetic field lines define the boundary of a polar cap on neutron star surface, which reads,

$$(x_{*,\text{lof}}, y_{*,\text{lof}}) = R_* \theta_{*,\text{lof}} (\cos \phi, \sin \phi). \quad (3)$$

Here,  $\theta_{*,\text{lof}} = \arcsin(\sqrt{R_*/r_{e,\text{lof}}})$ , which varies with the phases of magnetic field line planes. The shape of the polar cap is shown in Figure 3 for different inclination angles for a pulsar with a rotating period of 0.5s. The polar cap has a size of about 200 m but is compressed in the meridinal plane due to the inclination of the magnetic axis from the rotation axes. The polar cap calculated via the projection method is used in the following simulations.

##### 3.1.2. Distribution of relativistic particles

Relativistic particles are believed to be generated by sparking processes at polar caps above the neutron star surface. It

has been suggested that only some selected regions of the polar cap can spike rather than the entire cap. The preferred region might be organized in a central core and/or conal shape (Ruderman & Sutherland 1975). The density and distribution of particles are much uncertain, although there are many simulations (e.g. Cruz et al. 2021; Philippov & Kramer 2022). We assume that a bundle of particles is symmetrically distributed around the magnetic axis in a Gaussian shape,

$$f_e(r, \theta, \phi) = \frac{f_0}{r^3} \exp \left[ -\frac{(\theta_*/\theta_{*,\text{lof}})^2}{2\sigma_\theta^2} \right]. \quad (4)$$

Here,  $f_0$  is a normalization constant,  $\theta_* = \arcsin(\sin \theta \sqrt{R_*/r})$  and represents the polar angle of a field line footed on the neutron star surface,  $\theta_*/\theta_{*,\text{lof}}$  ranges from 0 to 1 and here  $\theta_{*,\text{lof}}$  varies with the azimuth angle  $\phi$  (see Figure 3),  $\sigma_\theta$  is the standard deviation for the distribution. The particle density scales with  $r$  by following  $1/r^3$ , similar as the Goldreich-Julian density (Goldreich & Julian 1969). The particles are assumed to have a fixed Lorentz factor  $\gamma$ , since their energy loss caused by curvature radiation is negligible compared to the particle energy itself.

### 3.1.3. Emission mechanism

Relativistic electrons and positrons are injected into the magnetosphere from the polar cap. In the near magnetosphere, the magnetic fields are extremely strong and the life time for any transverse movement is negligibly small. Relativistic particles stream along the curved magnetic field lines and experience curvature radiation. In the far magnetosphere with weak magnetic field, relativistic particles would have pitch angles with respect to the magnetic field lines. The synchro-curvature radiation is the probable mechanism for the radiation (Zhang & Cheng 1995).

Considering a relativistic particle bunch that has charge  $q$  and locates at the position  $\mathbf{r}$  in a magnetosphere, with the instantaneous trajectory approximated by  $\mathbf{r}_c$  in the circular path approximation, one can get the radiating electric field generated by these relativistic particles at frequency  $\omega$  in direction  $\mathbf{n}$  reads (Jackson 1975),

$$\mathbf{E}(\omega) = \frac{qe^{i\omega R_0/c}}{\sqrt{2\pi c R_0}} \int_{-\infty}^{\infty} \frac{\mathbf{n} \times [(\mathbf{n} - \mathbf{v}) \times \mathbf{a}]}{(1 - \mathbf{n} \cdot \mathbf{v})^2} e^{i\omega(t - \mathbf{n} \cdot \mathbf{r}_c)/c} dt. \quad (5)$$

Here,  $\mathbf{v}$  and  $\mathbf{a}$  represent the velocity in units of light speed  $c$  and the acceleration of the relativistic particle bunch.  $R_0$  is the distance from the circular path center to observer. For a movement along a field line,  $\mathbf{r}_c$ ,  $\mathbf{v}$  and  $\mathbf{a}$  can be found from Equations (11), (4) and (7) in Wang et al. (2012). In the current simulation, we set the rotation velocity to be zero, i.e.,  $v_r = 0$ , for the static magnetosphere.

Pulsar emission should be coherent as implied by its high brightness temperature. The coherence might be caused by plasma waves that arrange electrons and positrons in phase like an antenna. When the arranged particles move along the curved magnetic field lines, the coherent curvature emission is generated (Cheng & Ruderman 1977; Gangadhara et al.

2021). Due to coherence, the emission intensity scales as  $N^2 E^2(\omega)$  instead of  $N E^2(\omega)$ , with  $N$  representing the number of arranged particles. In our simulation, the coherence is treated by taking  $q = f_e e$  in Eq.(5), and hence the emission intensity  $\propto f_e^2$  in Eq.(4). The emission intensity can be represented by the Stokes parameters via  $I = E_x E_x^* + E_y E_y^*$ ,  $Q = E_x E_x^* - E_y E_y^*$ ,  $U = 2\text{Re}[E_x^* E_y]$  and  $V = 2\text{Im}[E_x^* E_y]$ . Here,  $E_x$  and  $E_y$  are the two projected components of  $E(\omega)$  in Eq.(5) on the x and y axes.

### 3.2. Steps for simulations

We simulate radio emission from the pulsar magnetosphere and project it to the sky in the following steps.

1. *Set up the pulsar magnetosphere:* For a pulsar with a given period  $P$  and an inclination angle  $\alpha$ , the geometry and the distribution of relativistic particles in the whole magnetosphere are set up following the assumptions given in sections 3.1.1 and 3.1.2. At any location given by the coordinates  $r$ ,  $\theta$  and  $\phi$ , the density of relativistic particles  $f_e$ , their velocity  $\mathbf{v}$  and acceleration  $\mathbf{a}$  can be determined.

2. *Link the emission from a magnetic field tangent to the sky:* For a pulsar rotating at phase  $\phi_1$ , the emission generated at a height  $r_0$  can be directed to a position in the sky. An observer in the sky defined by the line of sight  $\mathbf{n}$  can best receive the emission when  $\mathbf{n} \cdot \hat{\mathbf{v}} = 1$ , due to relativistic beaming effect. The coordinate for the tangential emission point ( $r_0$ ,  $\theta_0$  and  $\phi_0$ ) can be constrained by solving the equation.

3. *Calculate emission for particles within a cone of  $1/\gamma$ :* The emission of a relativistic particle or a particle bunch is beamed primary in a cone with a size of  $1/\gamma$  around  $\mathbf{v}$ . An observer in the sky at  $\mathbf{n}$  can detect the emission from the cone. Therefore, the radiating electric field is calculated using Equation 5 and the polarized emission is the incoherent sum of emission from the  $1/\gamma$  cone of all particle bunches.

4. *Get emission from the whole magnetosphere:* Radio emission at a given frequency can be generated from particles in a broad height region. We calculate the emission at a series of frequencies from all heights in pulsar magnetosphere.

5. *Project the emission onto the sky:* The emission at any frequency generated at any position inside the magnetosphere is projected onto the whole sky. An observer with a given line of sight receives the integrated emission from a series of  $1/\gamma$  emission cones around all tangent points in the magnetosphere. The emission beams with larger intensities can be identified from the sky distribution of the summed emission.

6. *Rotate the pulsar and get a profile for a given line of sight:* When a pulsar rotates, the projected emission in the sky rotates. In the observer's frame, the line of sight impacts the rotating sky in a given direction, and a pulse profile is obtained.

### 3.3. Results

By adopting the assumptions in Sect. 3.1 and following the steps in Sect. 3.2, we obtain the sky maps for radio emission from the whole magnetosphere. They exhibit diverse emis-

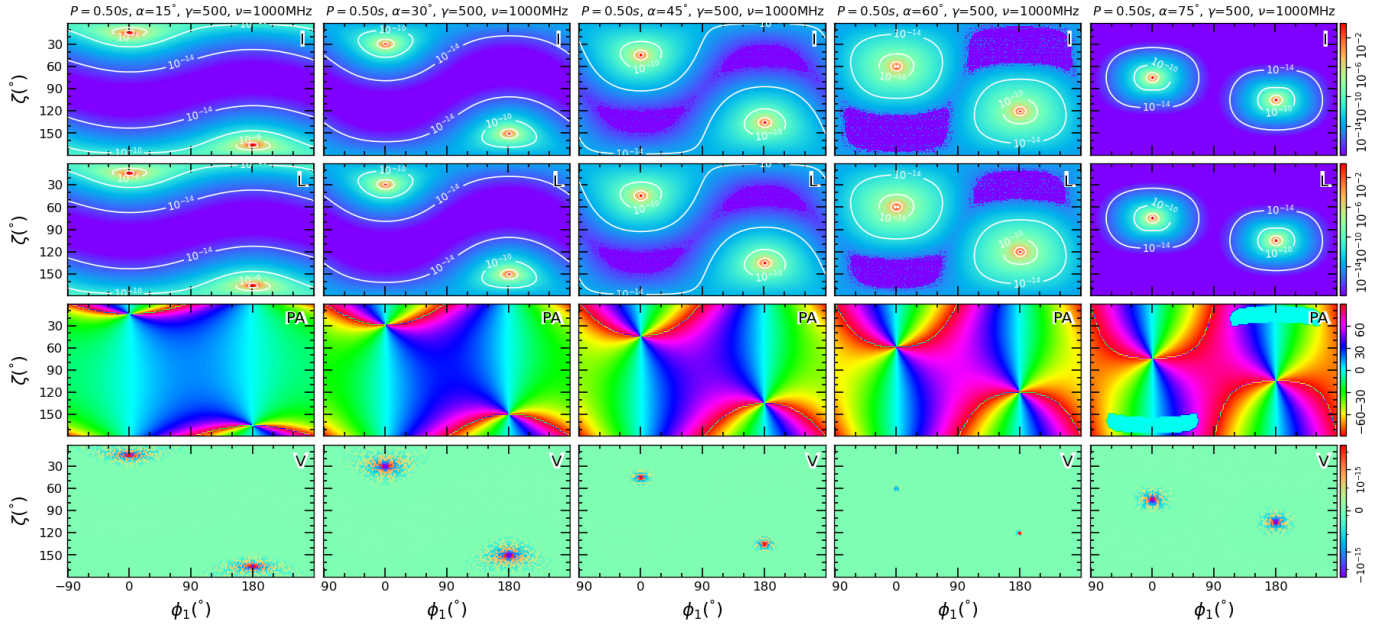


**Figure 4.** The Sky distribution of polarization emission intensity of a pulsar with different inclination angles  $\alpha = 15^\circ, 30^\circ, 45^\circ, 60^\circ$  and  $75^\circ$  (from left to right, as marked on the top). The distribution of the total intensity  $I$ , linear polarization  $L$ , polarization position angles  $PA$ , and circular polarization  $V$  are presented from the top rank to the bottom. The other parameters used for simulations are  $P = 0.5s$ ,  $\gamma = 500$ ,  $\sigma_\theta = 0.2$ , and  $\nu = 1000$  MHz.

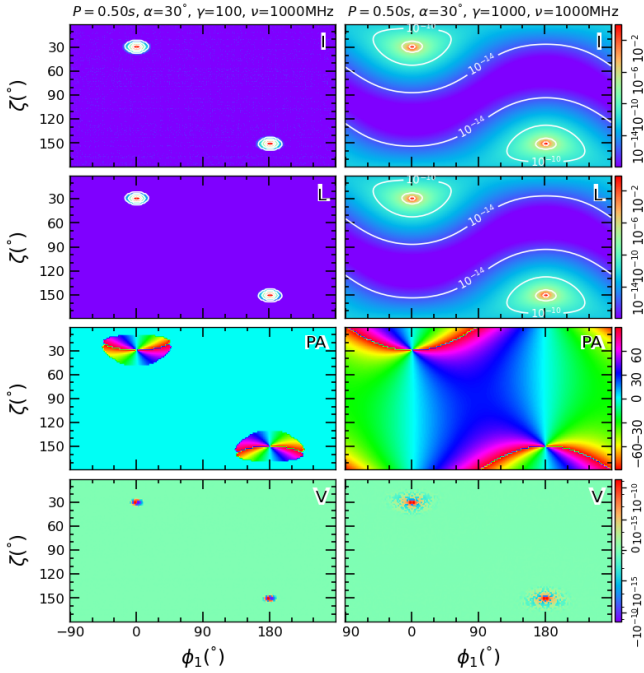


**Figure 5.** The same as Figure 4 but for relativistic particles with different Lorentz factors of 100 and 1000. The other parameters are fixed at  $P = 0.5s$ ,  $\alpha = 30^\circ$  and  $\nu = 1000$  MHz.

sion patterns, as shown in Figures 4, 5, and 6. When different lines of sight cut across these intensity distributions, various emission and pulse profiles can be detected, as shown in Figures 7 and 8. Indeed, one can have the radio emission across all rotation phases.

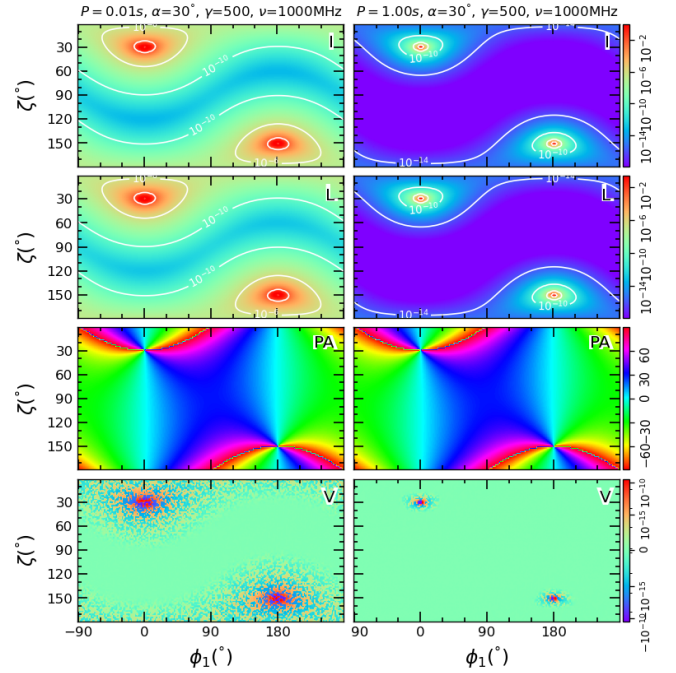


**Figure 6.** The same as Figure 4 but for different pulsar period of 0.01s and 1.0s. The other parameters are fixed at  $\alpha = 30^\circ$ ,  $\gamma = 500$  and  $\nu = 1000$  MHz.

### 3.3.1. Patterns in the intensity distribution of emission generated from the whole magnetosphere

Distributions of summed emission from the whole magnetosphere are shown in Figure 4 for pulsars with different in-

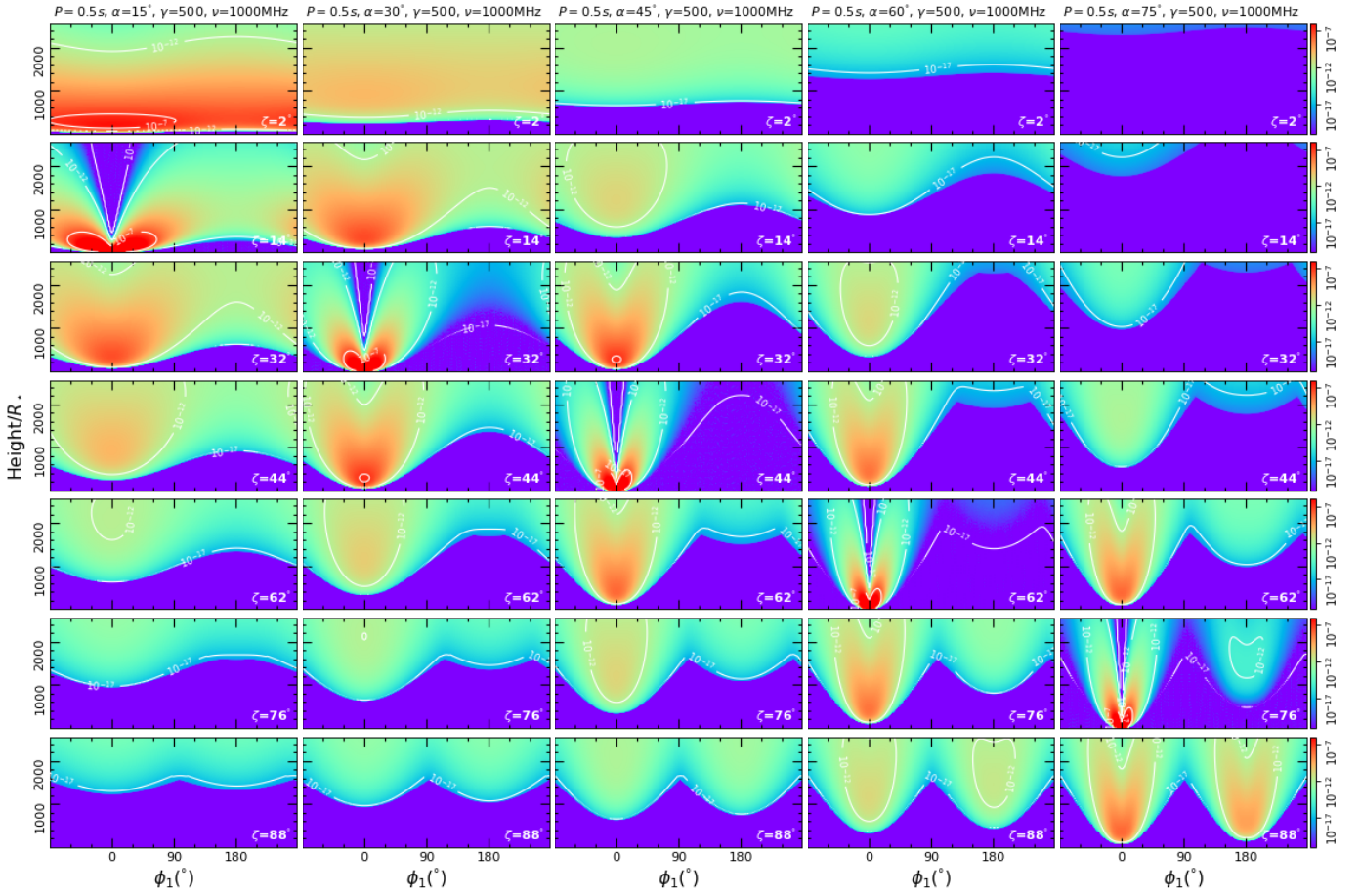


**Figure 7.** Simulated intensity distribution generated from different heights (the Y-axis) at different rotation phases (the X-axis) for different inclination angles of  $\alpha = 15^\circ, 30^\circ, 45^\circ, 60^\circ$  and  $75^\circ$  (from the left to right) and different angles for the line of sight  $\zeta = 2^\circ, 14^\circ, 32^\circ, 44^\circ, 62^\circ, 76^\circ$  and  $88^\circ$  (from the top to bottom). Other parameters used for simulations are the same as those in Figures 4.

clination angles. No question that the strong emission is generated around two magnetic poles. The linear polarization is about 80% the total intensity, and the position angles of linear polarization vary continuously with rotation phase. Because of the quasi-symmetric distribution of relativistic particles, the left and right-hand circular polarization are canceled seriously, so that the total circular polarization is only about  $10^{-9}$  of the total intensity.

Radio emission generated from the whole magnetosphere emerges at the entire rotation phases, despite with different inclination angles, though the intensity varies a lot. The emission at all phases is most preferably detectable by observers at a small angle from the rotation axis of a pulsar having a small inclination angle, i.e. viewing the almost aligned rotators near the pole. In such a case, the emission originates from one pole of the pulsar, e.g.,  $\zeta = 2^\circ$  for a pulsar with  $\alpha = 15^\circ$ . The emission at all phases might also be detected by an observer with the line of sight near  $\zeta \simeq 90^\circ$ , even though the emission is generated near the two poles of the quasi-orthogonal rotator, e.g.  $\alpha = 75^\circ$ .

The patterns of emission intensity distribution are different for pulsars having their magnetosphere filled by relativistic particles of different energies  $\gamma$ , as shown in Figure 5. The

emission beams surrounding both the magnetic poles are very small for a pulsar having less energetic particles, e.g. with Lorentz factor of 100, compared with the one having more energetic particles, e.g., with a Lorentz factor of 1000. This is because the more energetic particles remain to generate considerable curvature radiation from the higher magnetosphere where the curvatures of magnetic field lines are large. Moreover, polarization emission patterns are different for pulsars with different periods, as shown in Figure 6. The emission of a pulsar with a short period of 0.01s, which resembles a millisecond pulsar, has a much wide beam compared to a long period pulsar of e.g. 1.0 s. This is because the magnetic field lines are largely bent for the pulsars with shorter periods.

### 3.3.2. Polarized pulse profiles

When a given line of sight goes across the pulsar emission beam, the emission from a broad height range of pulsar magnetosphere can be detected. The emission intensity varies across heights, as shown in Figure 7. In general, the line of sight with small impact angles, i.e. a small  $|\zeta - \alpha|$ , can detect emission from the deep in the magnetosphere, as demonstrated by the emission detected by the line of sight of  $\zeta = 14^\circ, 32^\circ, 44^\circ, 62^\circ$  and  $76^\circ$  that cut pulsar emission

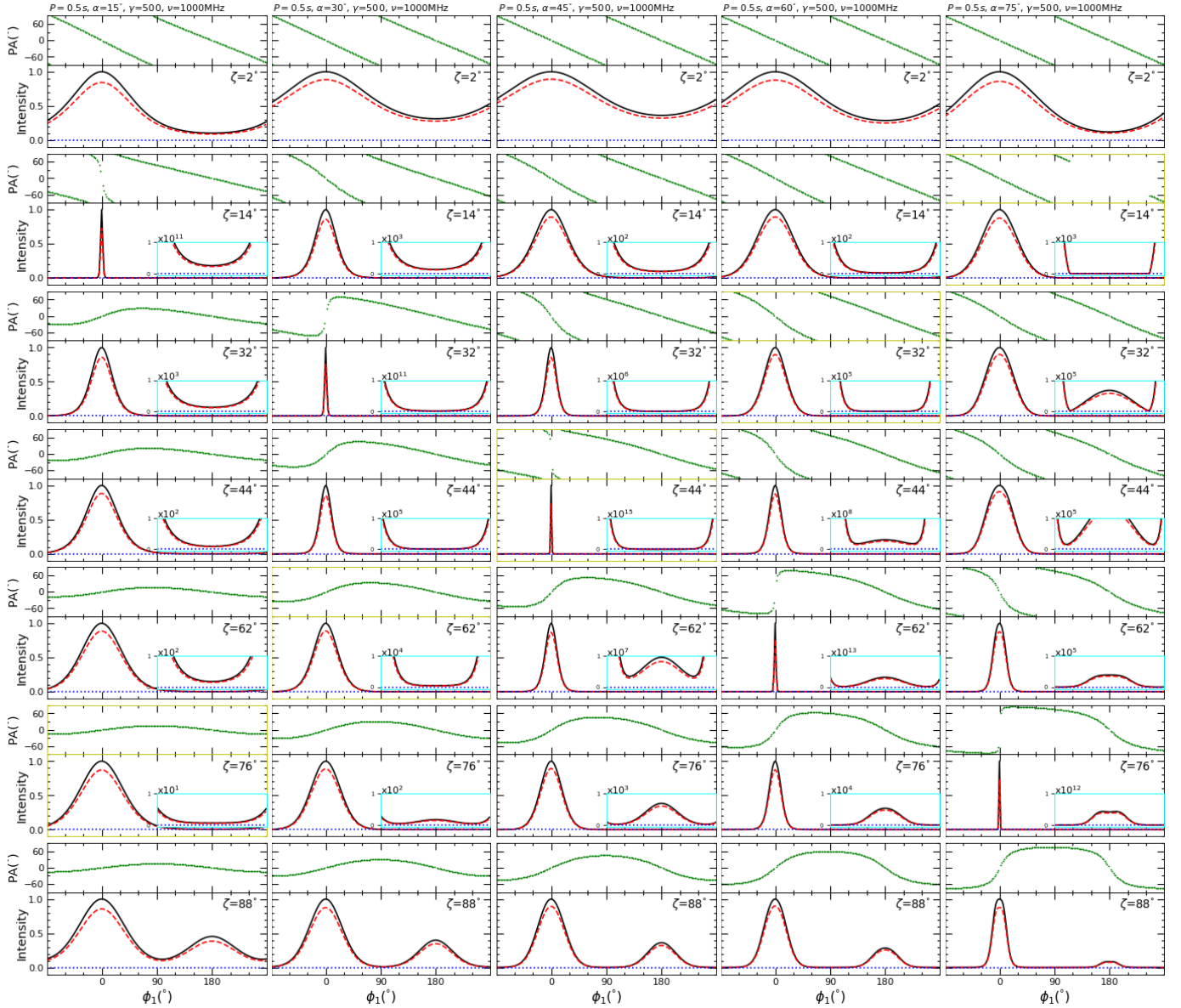


**Figure 8.** Pulsar polarization profiles from simulations with inclination angles of  $\alpha = 15^\circ, 30^\circ, 45^\circ, 60^\circ$  and  $75^\circ$  from the left to right and line of sight at  $\zeta = 2^\circ, 14^\circ, 32^\circ, 44^\circ, 62^\circ, 76^\circ$  and  $88^\circ$  from the top to the bottom. The total intensity  $I$ , linear polarization  $L$ , and circular polarization  $V$  are represented by solid black lines, red dashed lines, and blue dotted lines in the lower sub-panels and the polarization position angles are given in the upper sub-panels. The inserted sub-panels show the enlarged part for  $I$ ,  $L$  and  $V$  around the phase of  $\phi_1 = 180^\circ$ . These pulse profiles are calculated with the same sets of parameters as those in Figures 4 and 7.

beams with inclination angles of  $\alpha = 15^\circ, 30^\circ, 45^\circ, 60^\circ$  and  $75^\circ$ . If the detectable emission comes from the other pole, in general, a weak profile component emerges at a rotating phase of  $180^\circ$  from the main pulse, which is interpulse. When the impact angle gets larger, emission from higher regions in the pulsar magnetosphere can be detected, and the intensity contrast between the main pulse and interpulse becomes smaller.

Because of the symmetry of emission from two poles of the pulsar magnetosphere, only emission above the equatorial plane is shown in Figure 8. These polarized pulse profiles are obtained from the cutting of the emission patterns in Figure 4,

which is the sum of emission from all possible heights as shown in Figure 7. Radio emission from one magnetic pole is most likely detected for the pulsars with  $(\alpha + \zeta) < 90^\circ$ , as shown in the top-left sub-panels in Figure 8. For the pulsars with  $(\alpha + \zeta) > 90^\circ$ , radio emission from the two poles can be detected and the profiles are shown in the bottom-right sub-panels in Figure 8. The weak emission in the entire rotation phase therefore could be detected from either an aligned or an orthogonal rotating neutron star, with the line of sight of  $\zeta = 2^\circ$  or  $88^\circ$ , regardless of the impact angles to the magnetic axis.



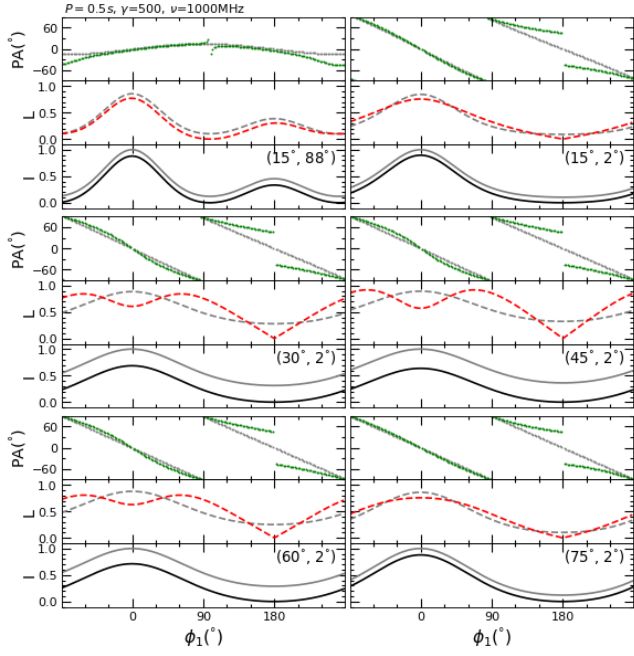


**Figure 9.** The same as Figure 8 but for polarized pulse profiles with persistent radio emission for pulsars with various geometries. If the persistent radio emission is not properly discounted, the  $L$  and  $PA$  curves would be distorted. The other parameters used for simulations are  $P = 0.5s$ ,  $\alpha = 30^\circ$ , and  $\nu = 1000$  MHz.

The gradients of position angle variations of polarized emission depend on the sign of impact angle of the line of sight. When the line of sight impacts the emission beam between the rotation and magnetic axes, i.e. the impact angle is negative, the polarization angles vary monotonically. When the line of sight impacts further than the magnetic axis with a positive  $\beta$ , as shown in Fig. 2, the polarization angle variations have different senses for the main pulse and interpulse, as shown in the bottom-right sub-panels in Figure 8. Vice versa for emission from the other hemisphere of pulsar magnetosphere.

Most striking is the persistent radio emission we obtained from the simulation, which is in addition to the pulsed radio emission and has not yet been considered in previous simulations. Generally, it is too weak to be detect for typical pulsar emission geometry. However, if the sight line is close to the rotation axes, e.g.,  $\zeta = 2^\circ$ , such a persistent emission can always be detected regardless of the inclination angle, for example  $\alpha = 15^\circ, 30^\circ, 45^\circ, 60^\circ$  or  $75^\circ$ , as shown in Figures 8. In addition, the persistent emission can be detected by sight lines with large angles, e.g.  $88^\circ$  for a pulsar with a small inclination angle of  $15^\circ$ . In practice, such a persistent emission can only be measured by using the sensitive synthesis telescope for source detection after the pulsed emission is excluded. Note that such persistent emission is highly polarized. When it is ignored, the obtained pulse profiles would have a bias in polarization, as shown in Figure 9.

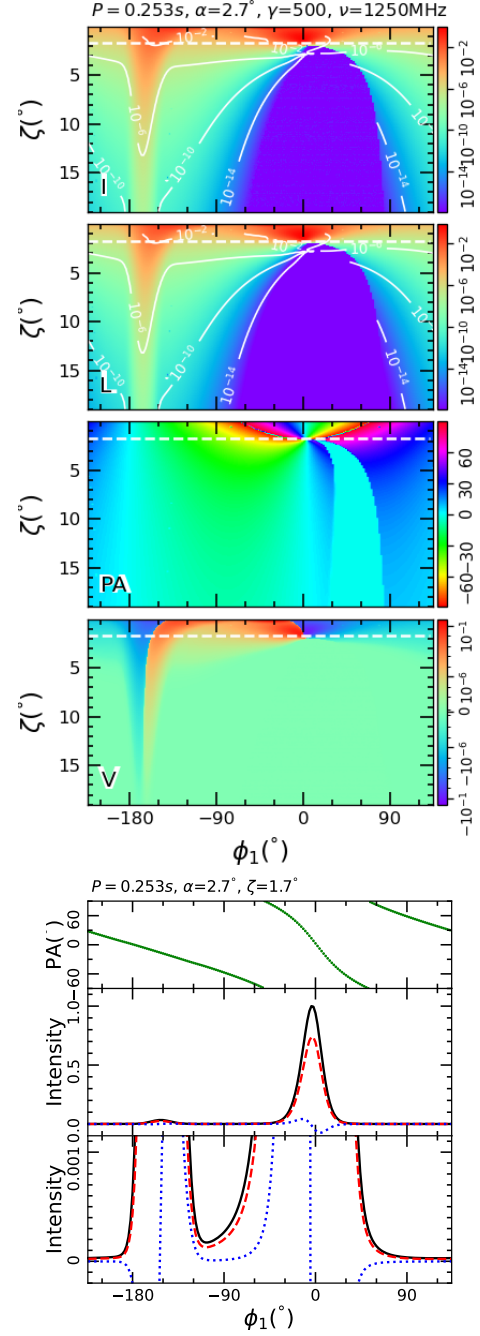


**Figure 10.** The specifically simulated sky distribution of polarization emission intensity for PSR J0953+0755 at 1250 MHz. The simulation assumes two bundles of relativistic particles with  $\gamma = 500$ . The sight line is at  $\zeta = 180^\circ - \zeta_0 = 1.7^\circ$ . The obtained polarized pulse profile is given in the lower panels, similar to the observed one in Figure 1.

#### 4. COMPARING MODEL WITH OBSERVATIONS

With the above simulations, one can see that the emission from all rotation phases can be generated. Here, we take simulations with specific parameters to generate the polarized radio emission mimic to the observed profiles of

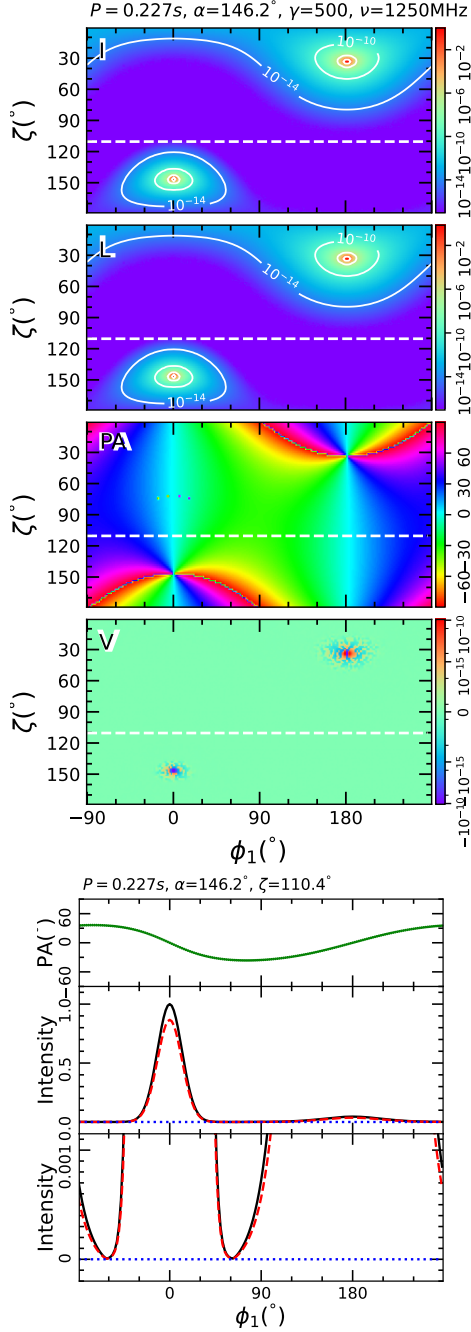


**Figure 11.** The same as Figure 10 but for PSR J1932+1059. The simulation assumes one bundle of relativistic particles with  $\gamma = 500$ . The sight line is at  $\zeta = 180^\circ - \zeta_0 = 110.4^\circ$ .

PSRs J0953+0755 from one pole of the magnetosphere and J1932+1059 from two poles.

Simulations for PSR J1932+1059 take the relativistic particles from both poles with the distribution defined by Eq. 4 and  $\sigma_\theta = 0.21$ . The sky distribution of the emission generated by these particles and the polarized pulse profile are shown in Figures 11. Simulations produced similar polarization profiles and PA curve as the observed ones. Due to

the symmetric distribution of particles around the magnetic axis, the circular polarization has the positive and negative senses canceled out. In fact, the FAST observations exhibit much more details for every individual pulses with intensity variations on short time scales and the diverse circular polarization and orthogonal modes. These features can not be reproduced by a simple model with a given set of parameters for a simple bundle of particles. All in all, our simulations reveal that emission can be generated in pulsar magnetosphere in all rotation phases.

## 5. DISCUSSION AND CONCLUSIONS

Sensitive radio observations show that pulsar emission emerges in the entire rotation phase. FAST observations of PSRs J0953+0755 and J1932+1059 have shown a huge dynamical ranges, and detected emission in some rotation phase down to less than 1/10000 the peak intensity. Their PA swings do not meet with the traditional RVM across the wide rotation phases. We developed a piecewise RVM which can be used to fit the PA values and get the emission geometrical parameters.

We have developed a theoretical model to understand the emission and polarization generated in the entire pulsar magnetosphere. We assumed the dipole geometry, symmetric distribution of relativistic particles, and the curvature emission mechanisms. The simulations have been carried out step by step, and the following conclusions can be derived:

1) Polarized radio emission can be generated in the entire rotation phases, though the intensity is much weak compared to the main emission beam around the magnetic poles. It is most likely produced by the pulsars having small periods and ones with the magnetosphere filled with much more relativistic particles.

2) The emission can be detected from the entire phase for two kinds of geometry. One is for the sight lines close to the rotation axis. Where the pulsed emission, together with the persistent radio emission, are detectable regardless of the inclination angle of a pulsar. The other is for the sight lines close to the equator, where emission from an orthogonal rotating neutron star is most likely to be detected.

3) Polarization angles of radio emission vary monotonically when the line of sight cuts the beam in between the rotation and magnetic axes. When the line of sight cuts the beam further than the magnetic axis, the senses of polarization position angle variation are opposite for the main pulse and interpulse.

4) The persistent radio emission is highly polarized. The pulsar polarization profiles would be distorted if such emission is ignored.

By assuming the energy and density distribution of relativistic particles and using the measured spin period and geometry parameters, we specifically simulate the polarized radio emission of PSRs J0953+0755 and J1932+1059. The model can matches observations for the main profile features.

Our model simulations only take the continuous injection of relativistic particles from the polar cap of the magnetic poles. Discrete injection due to sparking processes could lead

to variable emission features at different time scales. Instead of static magnetosphere, many effects have not yet considered, such as asymmetric as caused by rotational sweepback effect (e.g. Deutsch 1955; Dyks & Harding 2004), or polar cap currents (Hibschman & Arons 2001). In addition, the rotation itself has a great influence on the trajectory of particles and hence pulsar emission, as demonstrated by Blaskiewicz et al. (1991); Wang et al. (2012). Even after the emission is generated, the propagation effects can also significantly affect the observed polarization states (e.g. Melrose & Stoneham 1977; Wang & Lai 2007). Moreover, different profile components might originate from different heights of pulsar magnetosphere, as indicated by the relative phase shift  $d\phi_i$

from the piecewise RVM modelling. These influences should be considered together when the modeled polarization profiles is compared to the really observed ones from pulsars in future works.

We thank the referee for careful reading and helpful suggestions. P. F. Wang is supported by the National Natural Science Foundation of China (No. 12133004), National Key R&D Program of China (No. 2021YFA1600401 and 2021YFA1600400) and the National SKA program of China (No. 2020SKA0120200). J. L. Han is supported by the National Natural Science Foundation of China (No. 11988101).

## APPENDIX

### A. THE PIECEWISE RVM MODEL

For a given pulsar, a fixed set of geometry parameters, the inclination angle  $\alpha$  and the impact angle  $\beta$  or the sight line angle  $\zeta$ , can be determined by fitting the RVM to the observed position angle curve. However, for pulsars with wide profiles which have multiple widely spaced components generated from different heights in pulsar magnetosphere, one has to consider the aberration and retardation effects for different components, resulting in complex position angle swings. In fact, one can model the PA variation by using the following piecewise RVM function,

$$\psi = \begin{cases} \psi_0 + \arctan\left[\frac{\sin \alpha \sin(\phi - \phi_0)}{\sin \zeta \cos \alpha - \cos \zeta \sin \alpha \cos(\phi - \phi_0)}\right] & \text{(for main pulse),} \\ \psi_0 + \arctan\left[\frac{\sin \alpha \sin(\phi - \phi_0 - d\phi_i)}{\sin \zeta \cos \alpha - \cos \zeta \sin \alpha \cos(\phi - \phi_0 - d\phi_i)}\right] & \text{(for } i \text{ th component),} \\ \pi/2 + \psi_0 + \arctan\left[\frac{\sin \alpha \sin(\phi - \phi_0 - d\phi_j)}{\sin \zeta \cos \alpha - \cos \zeta \sin \alpha \cos(\phi - \phi_0 - d\phi_j)}\right] & \text{(for } j \text{ th component with orthogonal mode).} \end{cases} \quad (\text{A1})$$

Here,  $\alpha$ ,  $\zeta$ ,  $\phi_0$  and  $\psi_0$  have the same meaning as the traditional RVM and can depict the PA of the main pulse component.  $d\phi_i$  and  $d\phi_j$  represent the relative phase shifts of the  $i$ th and  $j$ th profile components with respect to the main one in the model. If the PA of the  $j$ th component exhibits orthogonal mode jump with respect to the main pulse, a shift of  $\pi/2$  is added to  $\psi$ .

We make use of the python packages, EMCEE and CORNER, and apply Equation A1 to the observed data to get the estimated parameters. As shown in Figure A1, we model PA variations of the three phase ranges for PSR J0953+0755 ( $C_0$ ,  $C_1$  and  $C_2$  marked in Figure 1) and get the marginalized probability distributions of the parameters. Similar fitting has been made for PSR J1932+1059 as well, as shown in Figure A2 for the four components ( $C_0$  to  $C_3$  marked in Figure 1).

## REFERENCES

- Arons, J., & Barnard, J. J. 1986, ApJ, 302, 120  
 Beskin, V. S., & Philippov, A. A. 2012, MNRAS, 425, 814  
 Biggs, J. D. 1990, MNRAS, 245, 514  
 Bilous, A. V., Griebmeier, J. M., Pennucci, T., et al. 2022, A&A, 658, A143  
 Blaskiewicz, M., Cordes, J. M., & Wasserman, I. 1991, ApJ, 370, 643  
 Cheng, A. F., & Ruderman, M. A. 1977, ApJ, 212, 800  
 Ching, T. C., Li, D., Heiles, C., et al. 2022, Nature, 601, 49  
 Cruz, F., Grismayer, T., Chen, A. Y., Spitkovsky, A., & Silva, L. O. 2021, ApJL, 919, L4  
 Desvignes, G., Kramer, M., Lee, K., et al. 2019, Science, 365, 1013  
 Deutsch, A. J. 1955, Annales d’Astrophysique, 18, 1  
 Dyks, J. 2008, MNRAS, 391, 859  
 Dyks, J., & Harding, A. K. 2004, ApJ, 614, 869  
 Everett, J. E., & Weisberg, J. M. 2001, ApJ, 553, 341  
 Gangadhara, R. T. 2004, ApJ, 609, 335  
 —. 2010, ApJ, 710, 29  
 Gangadhara, R. T., Han, J. L., & Wang, P. F. 2021, ApJ, 911, 152  
 Gautam, T., Ridolfi, A., Freire, P. C. C., et al. 2022, A&A, 664, A54  
 Gil, J. A., & Han, J. L. 1996, ApJ, 458, 265  
 Gil, J. A., & Snakowski, J. K. 1990, A&A, 234, 237  
 Goldreich, P., & Julian, W. H. 1969, ApJ, 157, 869  
 Gould, D. M., & Lyne, A. G. 1998, MNRAS, 301, 235  
 Han, J. L., Demorest, P. B., van Straten, W., & Lyne, A. G. 2009, ApJS, 181, 557  
 Han, J. L., & Manchester, R. N. 2001, MNRAS, 320, L35

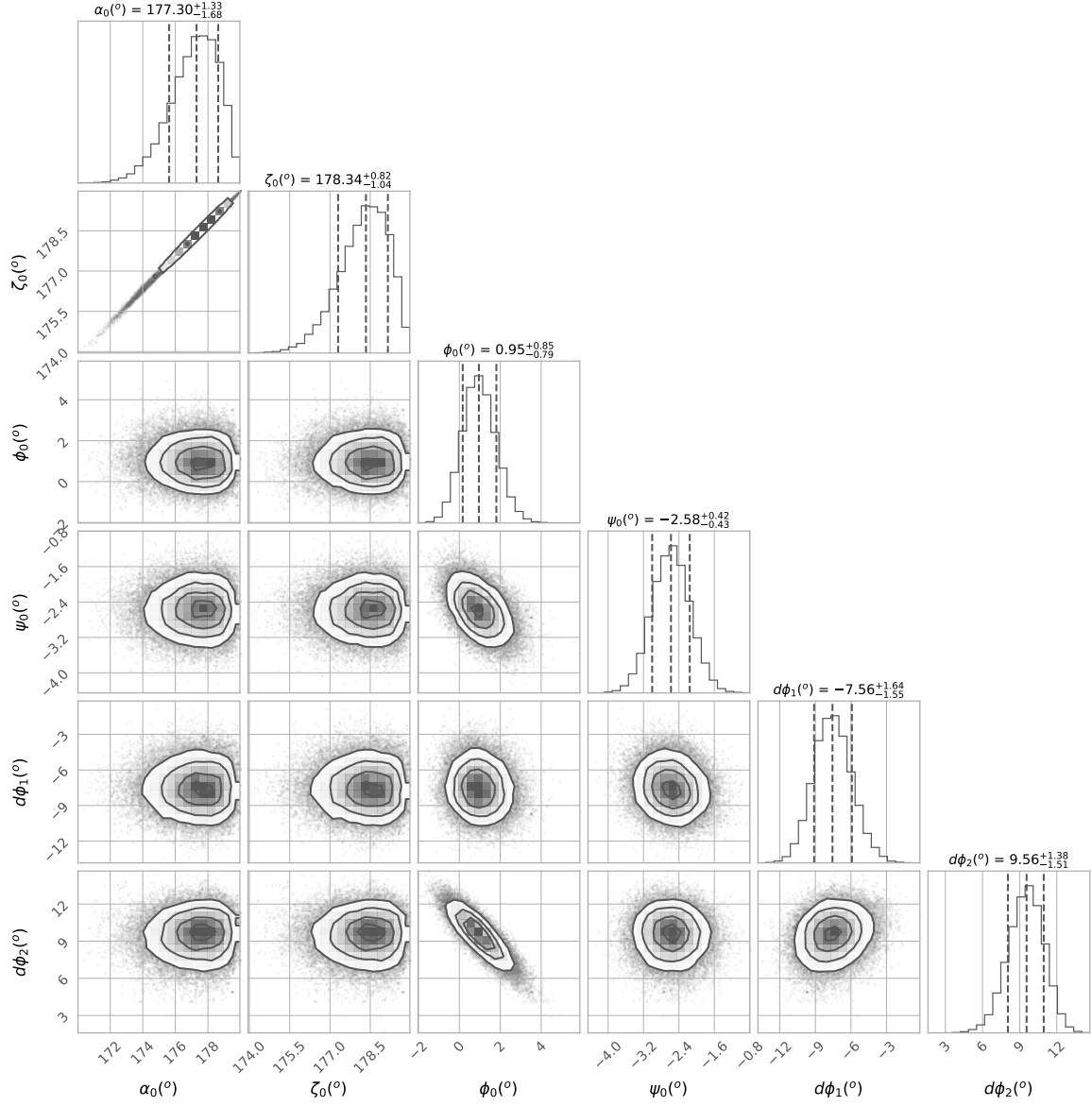


**Figure A1.** Marginalized probability distribution of the geometry parameters of PSR J0953+0755. The three dashed lines are for 16%, 50% and 84% of the samples in the marginalized distributions for each parameter. From which, the parameter values and their uncertainties are estimated, as indicated at the top for each parameter.

Hankins, T. H., & Cordes, J. M. 1981, *ApJ*, 249, 241

Hibschman, J. A., & Arons, J. 2001, *ApJ*, 546, 382

Jackson, J. D. 1975, *Classical electrodynamics*

Jiang, P., Tang, N.-Y., Hou, L.-G., et al. 2020, *RAA*, 20, 064

Kou, F. F., Yan, W. M., Peng, B., et al. 2021, *ApJ*, 909, 170

Large, M. I., Vaughan, A. E., & Wielebinski, R. 1968, *Nature*, 220, 753

Lyne, A. G., & Manchester, R. N. 1988, *MNRAS*, 234, 477

McLaughlin, M. A., & Rankin, J. M. 2004, *MNRAS*, 351, 808

Melrose, D. B., & Stoneham, R. J. 1977, *Proceedings of the Astronomical Society of Australia*, 3, 120

Nan, R. 2006, *Science in China: Physics, Mechanics and Astronomy*, 49, 129

Narayan, R., & Vivekanand, M. 1982, *A&A*, 113, L3

—. 1983, *ApJ*, 274, 771

Perry, T. E., & Lyne, A. G. 1985, *MNRAS*, 212, 489

Philippov, A., & Kramer, M. 2022, *ARA&A*, 60, 495

Phillips, J. A. 1990, *ApJL*, 361, L57

Pilkington, J. D. H., Hewish, A., Bell, S. J., & Cole, T. W. 1968, *Nature*, 218, 126

Posselt, B., Karastergiou, A., Johnston, S., et al. 2023, *MNRAS*, 520, 4582

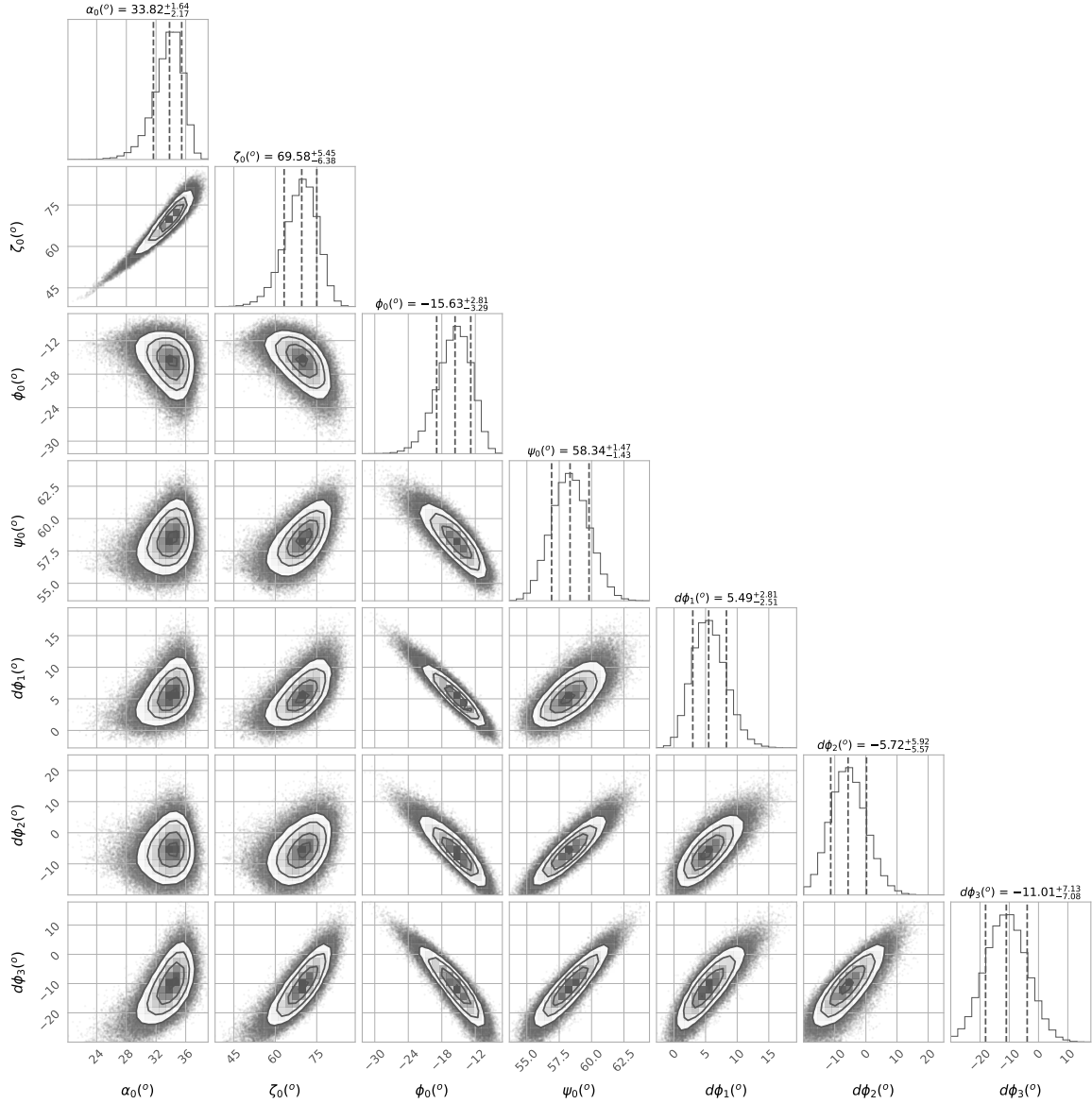


**Figure A2.** Same as Figure A1 but for PSR J1932+1059 with four components modelled.

Qiao, G. J., Lee, K. J., Wang, H. G., Xu, R. X., & Han, J. L. 2004, *ApJL*, 606, L49  
 Radhakrishnan, V., & Cooke, D. J. 1969, *Astrophys. Lett.*, 3, 225  
 Rankin, J. M. 1983, *ApJ*, 274, 333  
 —. 1993, *ApJS*, 85, 145  
 Rankin, J. M., & Rathnasree, N. 1997, *Journal of Astrophysics and Astronomy*, 18, 91  
 Ruderman, M. A., & Sutherland, P. G. 1975, *ApJ*, 196, 51  
 Stairs, I. H., Thorsett, S. E., & Camilo, F. 1999, *ApJS*, 123, 627  
 von Hoensbroech, A., & Xilouris, K. M. 1997, *A&A*, 324, 981  
 Wang, C., & Lai, D. 2007, *MNRAS*, 377, 1095

Wang, C., Lai, D., & Han, J. 2010, *MNRAS*, 403, 569  
 Wang, H. G., Pi, F. P., Zheng, X. P., et al. 2014a, *ApJ*, 789, 73  
 Wang, P. F., Wang, C., & Han, J. L. 2012, *MNRAS*, 423, 2464  
 —. 2014b, *MNRAS*, 441, 1943  
 Wang, P. F., Han, J. L., Xu, J., et al. 2023, *Research in Astronomy and Astrophysics*, 23, 104002  
 Wang, Z., Lu, J., Jiang, J., et al. 2022, *MNRAS*, 517, 5560  
 Xu, R. X., Liu, J. F., Han, J. L., & Qiao, G. J. 2000, *ApJ*, 535, 354  
 Zhang, H., Qiao, G. J., Han, J. L., Lee, K. J., & Wang, H. G. 2007, *A&A*, 465, 525  
 Zhang, J. L., & Cheng, K. S. 1995, *Physics Letters A*, 208, 47